Massively Parallel Selection of NanoCluster Beacons

Yu-An Kuo, Cheulhee Jung, Yu-An Chen, Hung-Che Kuo, Oliver S. Zhao, Trung D. Nguyen, James R. Rybarski, Soonwoo Hong, Yuan-I Chen, Dennis C. Wylie, John A. Hawkins, Jada N. Walker, Samuel W. J. Shields, Jennifer S. Brodbelt, Jeffrey T. Petty, Ilya J. Finkelstein, and Hsin-Chih Yeh*

NanoCluster Beacons (NCBs) are multicolor silver nanocluster probes whose fluorescence can be activated or tuned by a proximal DNA strand called the activator. While a single-nucleotide difference in a pair of activators can lead to drastically different activation outcomes, termed polar opposite twins (POTs), it is difficult to discover new POT-NCBs using the conventional low-throughput characterization approaches. Here, a high-throughput selection method is reported that takes advantage of repurposed next-generation-sequencing chips to screen the activation fluorescence of ≈40 000 activator sequences. It is found that the nucleobases at positions 7–12 of the 18-nucleotide-long activator are critical to creating bright NCBs and positions 4–6 and 2–4 are hotspots to generate yellow–orange and red POTs, respectively. Based on these findings, a "zipper-bag" model is proposed that can explain how these hotspots facilitate the formation of distinct silver cluster chromophores and alter their chemical yields. Combining high-throughput screening with machine-learning algorithms, a pipeline is established to design bright and multicolor NCBs in silico.

1. Introduction

Activatable and multicolor fluorescent probes are indispensable tools in analytical chemistry and quantitative biology as they enable sensitive detection of analytes and diagnostic imaging of biomarkers in complex environments.[1] Whereas activatable probes have greatly simplified the assays by eliminating the need to remove unbound probes, the development of new activatable probes is largely constrained by the scarce activation mechanisms (e.g., fluorescence resonance energy transfer (FRET)), the limited activation colors (e.g., existing FRET pairs), and the poor enhancement ratios (e.g., 10- to 60-fold for a typical molecular beacon).[2] NanoCluster Beacons (NCBs)[3] are a unique class of activatable probes as they provide a palette of activation colors from the same dark origin[4] (not via FRET) and achieve fluorescence enhancement ratios as high as 1500-[5] to 2400-fold.[6] The core of an NCB is a few-atom silver nanocluster[7] (e.g., Ag_8, Ag_{10}, or Ag_{16}) whose fluorescence can be tuned by its surrounding nucleobases.[7b,c,8] To create an NCB, a dark silver nanocluster (AgNC) is first synthesized in a C-rich DNA host (termed the NC probe), and a G-rich overhang (termed the activator) is brought into close proximity of the AgNC (via target-probe hybridization, Figure S1, Supporting Information) to activate its fluorescence (**Figure 1A,B**).[3–5,8a,d]

Y.-A. Kuo, Y.-A. Chen, O. S. Zhao, T. D. Nguyen, S. Hong, Y.-I. Chen, H.-C. Yeh
Department of Biomedical Engineering
University of Texas at Austin
Austin, TX 78712, USA
E-mail: tim.yeh@austin.utexas.edu

C. Jung
Department of Biotechnology
College of Life Sciences and Biotechnology
Korea University
Seoul 02841, Korea

H.-C. Kuo, J. R. Rybarski, I. J. Finkelstein
Department of Molecular Biosciences
University of Texas at Austin
Austin, TX 78712, USA

H.-C. Kuo, J. R. Rybarski, I. J. Finkelstein
Center for Systems and Synthetic Biology
University of Texas at Austin
Austin, TX 78712, USA

D. C. Wylie
Computational Biology and Bioinformatics
Center for Biomedical Research Support
University of Texas at Austin
Austin, TX 78712, USA

J. A. Hawkins
European Molecular Biology Laboratory (EMBL)
69117, Heidelberg, Germany

J. N. Walker, S. W. J. Shields, J. S. Brodbelt
Department of Chemistry
University of Texas at Austin
Austin, TX 78712, USA

J. T. Petty
Department of Chemistry
Furman University
Greenville, SC 29617, USA

H.-C. Yeh
Texas Materials Institute
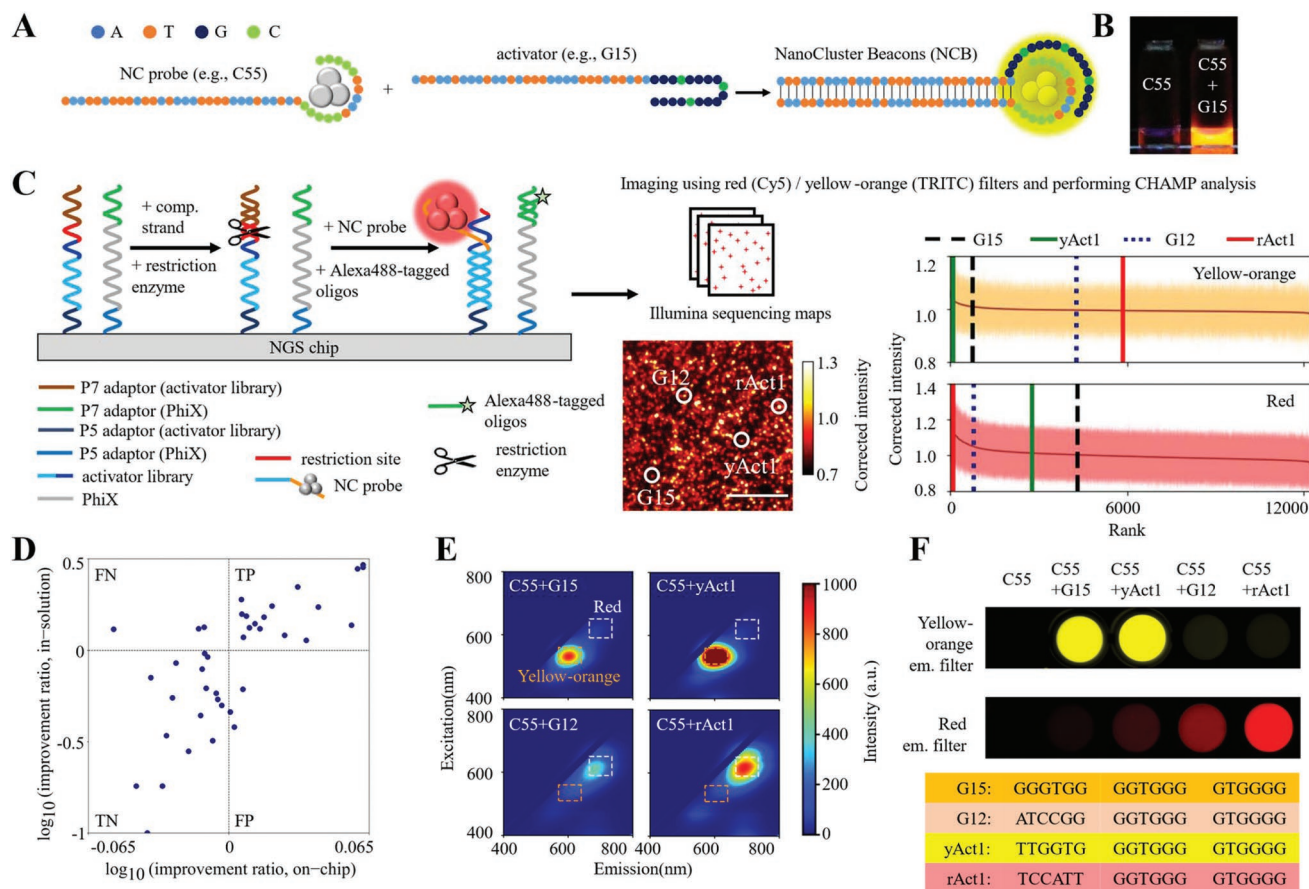University of Texas at Austin
Austin, TX 78712, USA

Figure 1. Massively parallel selection of NanoCluster Beacons (NCBs) using *MiSeq* chips. A) The interactions between a silver nanocluster (AgNC, left) and a proximal guanine-rich activator (middle) activate the fluorescence of AgNC by hundreds to thousands fold, creating an activated NCB (right). Here a common C55 nanocluster (NC) probe is used for NCB selection and optimization. G15 is the canonical activator for yellow–orange NCB. B) C55 NC probe before and after activation by G15 activator, under UV excitation (365 nm). C) Workflow of our high-throughput NCB selection on a next-generation sequencing chip (NGS; *MiSeq*, Illumina). After sequencing a library of activators (>12 000) on the *MiSeq* chip, unwanted adapter sequence above the activator was cleaved by a restriction enzyme. The Alexa488-tagged fiducial marker probes and the C55 probes were then injected into the chip to hybridize with the PhiX markers and the library, and imaged sequentially under an epifluorescence microscope. A custom bioinformatics and imaging processing pipeline was employed to identify activator sequences behind each activated NCB spot. After ranking all activators based on their median intensity (baseline corrected) on the chip surface, we could clearly differentiate strong activators from weak ones in the yellow–orange (Ex/Em: 535/50, 605/70 nm) and red (Ex/Em: 620/60, 700/75 nm) emission channels. Here, G15 and G12 were the standards (the known best NCBs) for the yellow–orange and red NCB comparisons, respectively. G15 and G12 were both ranked within top 7% among the yellow–orange and red NCBs in library_1. D) 20 activators from the 827 activators that were brighter than G12 (ranked 828th) and 20 activators from the 11 458 activators that were darker than G12 were investigated in test tubes using traditional fluorometry. The *MiSeq* results were 85% accurate in both true positive (TP) and true negative (TN) selections. Definition of the improvement ratio can be found in the methods. E) 2D spectra of the four representative NCBs in the yellow–orange (orange dashed box) and red (white dashed box) emission channels. Through fluorometry characterization, we found yAct1 to be 2.03-fold brighter than G15 and rAct1 to be 2.94-fold brighter than G12. Intensities were calculated based on a volumetric integral shown in Figure S2, Supporting Information. F) Plate-reader images acquired using yellow–orange (top) and red (bottom) excitation/emission filter sets, and the sequences of the four representative bright NCBs.

Being a low-cost probe that can be easily prepared in a single-pot reaction at room temperature,[7a] NCBs have been applied to the detection of nucleic acids,[8a,d,9] proteins,[10] small molecules,[11] enzyme activities,[8c] and cancer cells.[12]

Whereas new applications of NCBs are emerging across a broad range of disciplines, it is unclear what sequence features of the activators ultimately control the enhancement ratio and activation color of an NCB. To answer this fundamental question and to unleash the power of NCB in biosensing, we design and study "polar opposite twin" NCBs (hereafter, denoted as POT-NCBs). POTs are similar in appearance (i.e., sequence), but with very different personalities (i.e., fluorescence emissions).

In NCBs, POTs refer to a pair of NCBs that differ only by a single nucleotide in their activators, but have drastically distinct activation intensities or colors. Whereas POTs hold the key to understanding the NCB activation processes, there is no effective way to rapidly scan the vast activator sequence space and identify the most extreme POT-NCBs.

Here we repurpose next-generation sequencing (NGS) chips for high-throughput screening of fluorescent nanomaterials. In a single experiment, more than 10^4 activator mutations can be evaluated based on their capabilities in fluorescence activation of a common NC probe (C55 in Figure 1A). Although the fluorescence properties of tens to hundreds of silver nanocluster

species templated in short DNA strands can be studied in DNA microarrays[13] and robotic plates,[8b] less than 3000 DNA hosts have been investigated as of today using these methods. While NGS chips are repurposed for studying protein–nucleic acid interactions,[14] they have never been used for study, selection, and optimization of fluorescent nanomaterials. By screening more than 40 000 activator sequences on three Illumina *MiSeq* chips, we not only discover new NCBs that are brighter than the known best NCBs (G15 and G12) but also identify the positions of nucleobases that are key to stabilizing bright AgNC chromophores (termed the critical zone). In the search for the most extreme POTs, the chip platform helps pinpoint the single-nucleotide substitution hotspots for generating yellow–orange and red POT-NCBs, reaching 31- and 9-fold differences in the enhancement ratios, respectively (563 vs 18 for a pair of yellow–orange POTs and 285 vs 32 for a pair of red POTs). Based on the findings of the critical zone for hosting bright chromophores (positions 7–12) and the hotspots for generating POTs (positions 4–6 for yellow–orange POTs and positions 2–4 for red POTs), we propose a "zipper-bag" model that could explain how POT hotspots lead to the creation of distinct AgNC chromophores and alter the chromophore chemical yields. In addition, with proper selection of the sequence features, we build machine-learning models that can design yellow–orange and red NCBs in silico. NCBs designed using these tools are 8.5 and 2 times more likely to be bright yellow–orange and red, respectively, as compared to the ones with random activator sequences. Our high-throughput screening and machine-learning design pipeline is not only accelerating the discovery of new NCBs for diverse applications, but also providing insights into the chemical yield and the emitter brightness controlled by the sequence features.

2. Results

2.1. High-Throughput Selection of Red and Yellow–Orange NCBs on NGS Chips

In our first library design (library_1), the 18-nt-long canonical activator G15[3,4,8a,d] (GGGTGG GGTGGG GTGGGG) was divided into three 6-nt-long segments, and each segment was separately randomized to create $3 \times 4^6 - 2 = 12\,286$ activator mutations (two were G15 duplicates in the 3×4^6 combinations, Table S1, Supporting Information, and Experimental Section). This approach significantly reduced the library size from 4^{18} (the entire ligand composition space) down to $\approx 10^4$ in a single experiment. After mixing with the fiducial markers (PhiX), the library sequences were immobilized, bridge amplified, and sequenced on an Illumina *MiSeq* chip. As the sequencing-needed barcodes and adapters (i.e., SP2/barcode/P7 adapter, Table S1, Supporting Information) could suppress or alter the NCB fluorescence (Figure S3, Supporting Information), they were removed using a restriction enzyme, leaving behind 20-nt-long activators (the library) that were only 2 nt (a pair of CG dinucleotides) longer than the activators used in the traditional low-throughput test-tube selections[3,4,8a,d] (Figure 1C and Table S1, Supporting Information). After enzymatic cleavage, the quality of the library was checked by staining the library

with an Atto647N-labeled probe, before using the library for NCB selections (Figure S4, Supporting Information).

We first aimed to discover new activators that light up the common C55 NC probe (CCCCCTTAATCCCCC, which hosts a dark AgNC) more intensely than G15 in yellow–orange emission (within 570–640 nm). We also searched for activators that give distinct emission colors (e.g., red emission within 663–738 nm). The yellow–orange and the red emissions here were simply defined by the filter cubes (i.e., TRITC and Cy5) commonly used for fluorescence imaging. Our color channel definitions were different from those used in other AgNC research,[15] where the color definitions were due to some structural factors. Once the complementary AT sequences on the C55 probe and the activators hybridized, AgNC emission developed.[4,5] In the traditional test-tube experiments, the NC probe-activator mixtures were heated to 90–95 °C for a minute and gradually cooled down to room temperature to allow hybridization.[3,4] On the *MiSeq* chip, a constant temperature of 40 °C was maintained to enable hybridization (Figure S6, Supporting Information, and Experimental Section). This relatively low hybridization temperature extended the life of the chip, allowing us to go through at least 20 rounds of activation experiments on a single chip (hybridized with C55 probes, washed and imaged, and then removed C55 probes using an alkaline solution) without showing any degradation, thus providing highly reproducible selection results (Spearman's $\rho = 0.93 \pm 0.005$ for the red NCBs and 0.88 ± 0.024 for the yellow–orange NCBs, Figures S12 and S13, Supporting Information). We emphasize that when using 40 °C and 40 min for NCB hybridization in test tubes, the resulting fluorescence activation was indistinguishable from that carried out at 90 °C for 1 min (Figures S16 and S17 and Tables S3 and S4, Supporting Information).

After injecting the common C55 NC probes into the *MiSeq* chip, the chip was scanned using a wide-field fluorescence microscope equipped with a metal halide illuminator, a sCMOS camera, and an *xyz* translation stage. The activated NCBs were sequentially imaged using the filter cubes designed for conventional red emitters (e.g., Cy5, Ex/Em: 620/60, 700/75 nm) and yellow–orange emitters (e.g., TRITC, Ex/Em: 535/50, 605/70 nm). These two filter cubes were selected due to their popularity in fluorescence imaging. A custom bioinformatics and imaging processing pipeline[14d] was employed to identify activator sequences behind each activated NCB spot (Figure 1C). By ranking the activators based on their median intensity (baseline corrected; Experimental Section) on the chip surface (each activator had 457 ± 308 polonies on the *MiSeq* chip; Experimental Section), we could clearly distinguish strong activators from weak activators in the two emission channels (Figure 1C right).

Compared to other high-throughput screening methods that rely on fluorescence from single molecules for characterization,[16] photobleaching is not a severe issue in our approach, as each activator polony contains hundreds of activated NCBs. Polony is a contraction of "polymerase colony," which is a small colony of DNA amplified from a library sequence. By employing an autoscan algorithm and shutter control (Experimental Section), the excitation dose to each polony is precisely regulated, avoiding any uneven photobleaching and ensuring consistent imaging results. By acquiring a

Table 1. Sequence designs in library_1. In library_1, the 18-nt-long canonical activator G15 was divided into three 6-nt-long segments and each segment was separately randomized, creating a library with total 12,286 activators. "N" represents the canonical nucleobase A, T, G, and C. Consequently, each of the segment_1, segment_2, and segment_3 comprised of 4096 variants, while each of the segment_11 to segment_32 comprised of 64 variants.

Canonical		5'–GGGTGGGGTGGGGTGGGG–3'	
Segment_1, library_1	NNNNNNGGTGGGGTGGGG	Segment_11	NNNTGGGGTGGGGTGGGG
		Segment_12	GGGNNNGGTGGGGTGGGG
Segment_2, library_1	GGGTGGNNNNNNGTGGGG	Segment_21	GGGTGGNNNGGGGTGGGG
		Segment_22	GGGTGGGGTNNNGTGGGG
Segment_3, library_1	GGGTGGGGTGGGNNNNNN	Segment_31	GGGTGGGGTGGGNNNGGG
		Segment_32	GGGTGGGGTGGGGTGNNN

fluorescence image every 200 ms, an intensity time trace of each polony is obtained, which can be fitted with a single exponential decay. After 1 s of wide-field illumination (≈10 W cm^{-2}), polony intensity decreases by ≈20% at most (Figure S10, Supporting Information).

Based on the chip screening results, we randomly select 20 activators from the 827 activators that are brighter than G12 (ranked 828th) and 20 activators from the 11 458 activators that are darker than G12 for further investigation in test tubes by fluorometry. Using the G12 activator (ATCCGGGGTGGGGTGGGG) as the standard for red NCB comparison, the *MiSeq* chip screening results were 85% accurate in both true positive and true negative selections (brighter or darker than G12 in chip screening and confirmed in fluorometry, Figure 1D and Figures S14 and S15, and Table S2, Supporting Information). In particular, rAct1 (TCCATTGGTGGGGTGGGG) was found 2.94-fold brighter than G12 in the red channel (enhancement ratios were 1292 vs 439, Figure 1E and Figure S14 and Table S2, Supporting Information). We then evaluated the "spectral purity" of selected NCBs by computing the intensity ratio between the two colors. For the selected bright red NCBs, 70% of them were spectrally pure in red emission as their integrated intensity under the red window (663–738 nm) was at least 3.5-fold larger than that under the yellow–orange window (570–640 nm). When comparing the chip screening results with the test-tube results, a coefficient of determination of 0.50 was obtained (Figure 1D). We noticed the intensity differences found on *MiSeq* chips were substantially smaller than those found in test tubes (e.g., 1.20-fold red-emission difference was found between rAct1 and G12 NCBs on a *MiSeq* chip, but it became 2.94-fold in test tubes). The underestimation was attributed to the relatively higher fluorescence background on *MiSeq* chips and the variations in polony numbers among the library sequences (for instance, ≈240 activators had less than 30 polonies in library_1). Out of the twelve yellow–orange candidates, we found yAct1 (TTGGTGGGGTGGGGTGGGG) to be 2.03-fold brighter than G15 (the standard for yellow–orange NCB comparison) in activating C55 in the yellow–orange channel (enhancement ratios were 1,125 vs 553, Figure S17 and Table S4, Supporting Information). We emphasize that the small-scale investigations carried out in test tubes, such as single-nucleotide substitutions from G15 at each nucleobase position (totally 3 × 18 = 54 variants), would lead to an activator that is only 44% brighter than G15 (Figure S18, Supporting Information).

2.2. Identification of Critical Nucleobases in Stabilizing Bright AgNC Chromophores

The screening results from library_1 (**Table 1**) clearly indicated that segment_2 prefers to be conserved (GGTGGG) in order to maintain NCB brightness (**Figure 2**B). In contrast, randomizing segment_1 still produced many bright red NCBs, especially when segment_1 became C-rich. The effect of segment_3 was diverse, suggesting an indirect activation role. The 6-segment interrogation further revealed that segment_22 (positions 10–12) is more important than segment_21 (positions 7–9) in creating bright red NCBs (Figure 2C and Figure S20, Supporting Information). Independent investigations using library_2 and library_3 (≈28 000 frame-shifted activators, Table S1, Supporting Information) also confirmed that the nucleobases in positions 10–12 are critical in C55 activation (Figure S20, Supporting Information). These results indicated that bright AgNC chromophores are most likely "clamped" by the two strands at positions 7–12 (Figure 2A), possibly forming silver-mediated pairs between the two strands.[17]

Drawing from the Table 1 and Figure 2 results, one possible design rule for creating bright red NCBs on C55 is to develop an activator with a C-rich segment_1, a GC-rich segment_21, a G-rich segment_22, and a TC-rich segment_3. Nevertheless, the activator CCCCCCGCGGGGTTTCCC (termed G5) actually had a low red enhancement ratio (39, as compared to 439 for G12; Figure S22 and Table S9, Supporting Information). This result clearly indicated that segments do not work alone—cooperativities among the segments determine the activation color and intensity of an NCB. Whereas previous investigations showed that more guanines in the activator generally lead to brighter red emission,[3] our large-scale investigations revealed a different design rule—brighter red NCBs can be achieved with fewer numbers of guanines (e.g., 10G_5 in Figure S23 and Table S5, Supporting Information). As the results from our high-throughput screening could not be easily transformed into simple design rules, we trained machine-learning algorithms on the dataset and used them to design bright NCBs in silico.

2.3. Discovery of Polar Opposite Twins Using NGS Chips

Taking advantage of the chip screening platform, we searched for POT-NCBs that have the most extreme color or intensity differences (**Figure 3**A–C). Although NCBs were previously

**ADVANCED
SCIENCE NEWS**

www.advancedsciencenews.com
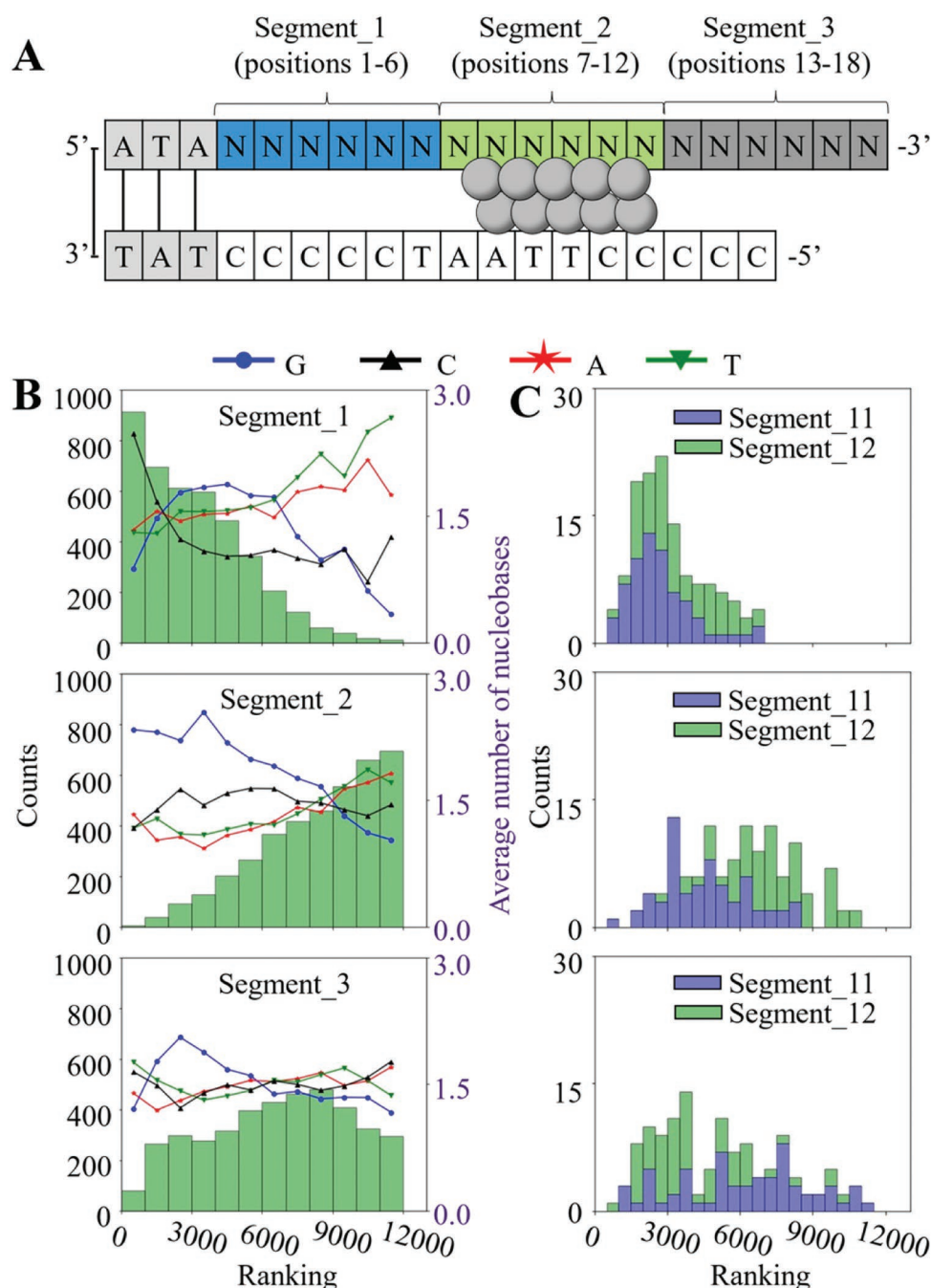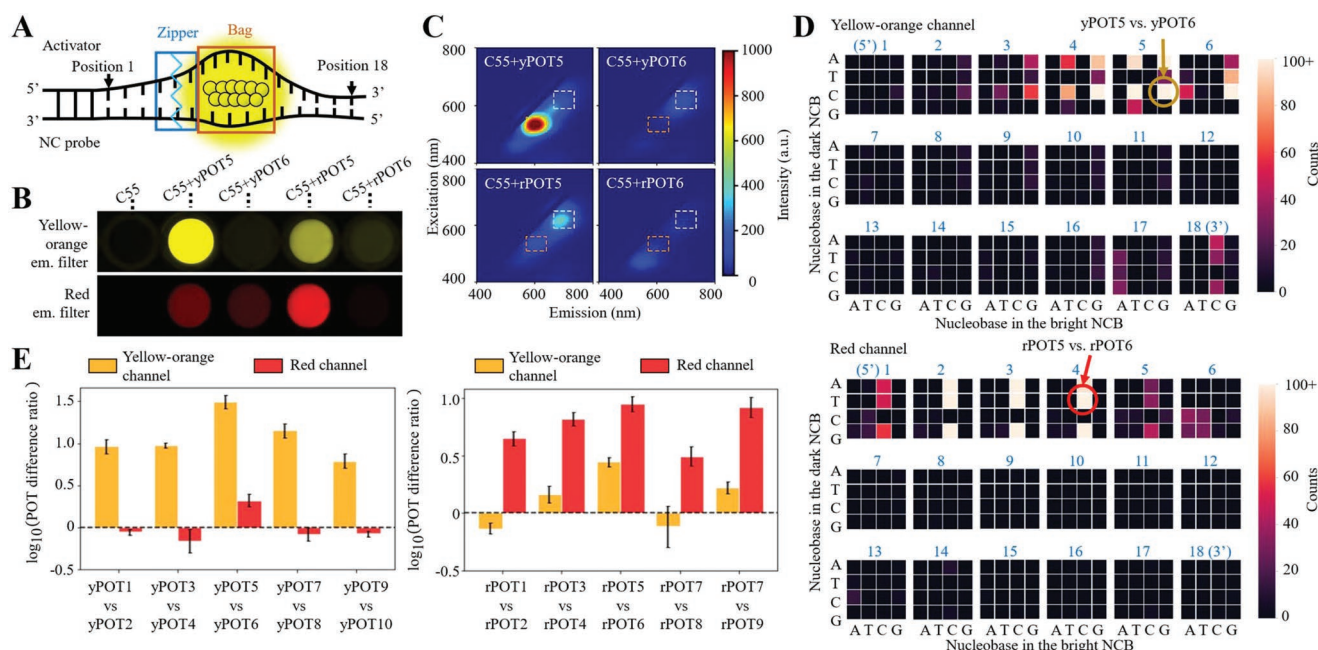
**ADVANCED
MATERIALS**

www.advmat.de

Figure 2. Influence of activator mutations on red NCB brightness. A) Schematic of NCB construct and definition of nucleobase positions in the activator. B) Histograms of the brightness rankings corresponding to the mutated segments and the average numbers of the four nucleobases in the mutated segments. The library_1 results clearly indicated that, to make a bright NCB, segment_2 (the middle six nucleobases, positions 7–12) prefers the canonical G-rich sequence, as randomizing segment_2 (while keeping segment_1 and _3 canonical) leads to many low-ranking NCBs in both emission channels. Each histogram here contained 4096 activators. C) Stacked histograms further demonstrated that segment_22 (positions 10–12) is more important than segment_21 (positions 7–9) in creating bright red NCBs.

used for single-nucleotide polymorphism detection,[4,8a] only tens of activators were tested, providing little information on the rules to design POTs. In contrast, library_1 alone contained more than 110 000 pairs of twin NCBs (Figure S24, Supporting Information), where the top 2000 pairs were readily candidates for POTs. Upon examining these 2000 pairs of twin

NCBs (Figure 3D), it was clear that the nucleobases in positions 4–6 are critical for creating yellow–orange POTs (e.g., bright [x-axis]→dark [y-axis] conversion by G/T→C/A substitution at position 5 and G→C substitution at positions 4 and 6), while the positions 2–4 are critical for creating red POTs (bright→dark conversion by C→ATG substitution). 15 top POT pairs were

Figure 3. Substitution hotspots to generate polar opposite twins (POTs) revealed by *MiSeq* chip selection. A) Schematic of the zipper-bag model. The blue box represents the "zipper" location (e.g., positions 4–6 for yellow–orange POTs) and the gray box represents the "bag" location (i.e., the critical zone at positions 7–12). When the zipper does not seal well, the bag is leaky, thus leading to a low chemical yield and dimmer NCB. B) Plate-reader images acquired using yellow–orange (top) and red (bottom) excitation/emission filter sets and the sequences of the representative POTs. Large differences in fluorescence enhancement ratios were seen in these twin NCBs (C55 + yPOT5 vs C55 + yPOT6 for yellow–orange channel, and C55 + rPOT5 vs C55 + rPOT6 for red channel), making them POTs. yPOT5: CAGTGAGGTGGGGTGGGG; yPOT6: CAGTCAGGTGGGGTGGGG; rPOT5: AATCCTGGTGGGGTGGGG; rPOT6: AATTCTGGTGGGGTGGGG. C) 2D spectra of the representative POTs in the yellow–orange (orange dashed box) and red (white dashed box) emission channels. D) Heat maps of the top 2000 twin NCB pairs in library_1. Here the *x*-axis and the *y*-axis represent bright to dark conversion in these twin NCBs. These heat maps clearly indicated that the nucleobases in positions 4–6 are critical for creating yellow–orange POTs, while the positions 2–4 are critical for creating red POTs. E) The POT difference ratios of five representative yellow–orange (left) and red (right) pairs of POTs in the two emission channels. Through fluorometry characterization, the yPOT5-yPOT6 pair and the rPOT5-rPOT6 pair were identified as the most extreme yellow–orange and red POTs, respectively, reaching POT difference ratios as high as 31 and 9. Definition of the POT difference ratio can be found in the methods. Error bars: mean ± standard deviation (s.d.) in logarithmic scale, with three repeats for each pair of POTs.

further investigated in test tubes. The most extreme yellow–orange and red POTs had 31-fold (yPOT5-yPOT6 with G→C substitution at position 5) and 9-fold (rPOT5-rPOT6 with C→T substitution at position 4) differences in their enhancement ratios, respectively (Figure 3E). For the ease of comparison, we termed the difference in the enhancement ratios in a pair of POT the "POT difference ratio" (Figures S25 and S26 and Tables S7 and S8, Supporting Information), where the pair with the largest POT difference ratio is the most extreme POT.

The POT difference ratio reflected the sample brightness difference at the ensemble level, which equaled the product of "chromophore chemical yield ratio" and "single-emitter brightness ratio." Using fluorescence correlation spectroscopy (FCS),[18] we found that the chromophore chemical yield of rPOT5 NCB was 5.46-fold higher than that of rPOT6 NCB (24.41% vs 4.47%), and the single-emitter brightness of rPOT5 was 1.64-fold higher than that of rPOT6 (5.67 vs 3.45 kHz, Figure S27, Supporting Information). The product of the 5.46× chromophore chemical yield ratio and the 1.64× single-emitter brightness ratio was indeed the 9× POT difference ratio measured by fluorometry. Similarly, the chromophore chemical yield of yPOT5 NCB was 16.33-fold higher than that of yPOT6 NCB (25.80% vs 1.58%) and the single-emitter brightness of yPOT5 NCB was 2.19-fold higher than that of yPOT6 NCB (7.04 vs 3.22 kHz, Figure S28,

Supporting Information). The product of the 16.33× chromophore chemical yield ratio and the 2.19× single-emitter brightness ratio was close to the 31× POT difference ratio measured at the ensemble level. Our investigation of POTs led to two important findings. First, the red AgNCs in rPOT5 and rPOT6 were actually different species as their excitation peak wavelengths (610 vs 605 nm, Figure S25A, Supporting Information), absorption spectra (a clear peak at 610 nm in rPOT5 NCBs spectrum but no clear peak in rPOT6 NCBs spectrum, Figure S29C, Supporting Information), and single-emitter brightness were all different. Second, the chemical yield of AgNC chromophores could be significantly altered by substituting single nucleobases at positions (2–6 in Figure 3D) outside the critical zone (7–12 in Figure 2A). Based on these findings, we proposed a zipper-bag model that could explain the mechanism behind POT formation (Figure 3A).

3. Discussion

3.1. Investigation of the Zipper-Bag Model

In our zipper-bag model, the bag is the critical zone (positions 7–12) that holds the AgNC chromophore while the

zipper is the POT hotspot that seals the bag. A subtle change in the zipper can alter the sealing condition of the zipper bag, which perturbs the short-range ligand environment around the AgNC inside the bag and possibly changes its binding footprint with the bag (Figure 3A). We have previously shown that by slightly shifting the position of the activator with respect to the NC probe, a new ligand environment can be created around the AgNC that alters its emission spectrum,[8a,d] and we believe such a nucleobase–AgNC interaction is within a short range (≤1 nm).[8a] When studying AgNC structures using 193 nm activated-electron photodetachment mass spectrometry (a-EPD MS), we have previously found that two Ag_{10} clusters can be completely distinct chromophores due to very different binding footprints in their DNA hosts.[19] The earlier structural studies by extended X-ray absorption fine structure spectra complemented the a-EPD MS footprint results.[7d,20] Here by using FCS, we further demonstrated that a change in zipper may result in not only a distinct AgNC chromophore in the bag but also a different chemical yield of the chromophore, thus providing a basis for POT formation.

It is noted that the zipper locations for the yPOT5-yPOT6 pair (at position 5) and the rPOT5-rPOT6 pair (at position 4) are different. One possibility is that red AgNC chromophores have higher silver stoichiometries and larger footprints in the bag, pushing the zipper locations (positions 2–4) further away from the bag (positions 7–12, Figure S25B, Supporting Information). Using electrospray ionization mass spectrometry (ESI-MS), Gwinn's group has previously shown a general trend for yellow chromophores having a smaller core (Ag_{10}–Ag_{11}) and red chromophores having a larger core (Ag_{14}–Ag_{16}).[7c] According to their rod-shaped model,[7b] red chromophores are expected to have larger footprints in their DNA hosts. However, in Gwinn's experiments, their AgNC chromophores are most likely stabilized inside dimers of 10-mers, whose ligand environments are different from our activator/NC probe systems.

To investigate the silver stoichiometries of the two major chromophores in our POT experiments, we purified yPOT5, yPOT6, rPOT5, and rPOT6 NCB samples using 20% native polyacrylamide gel electrophoresis (native PAGE) (Figure S30, Supporting Information, and Experimental Section) and analyzed the purified samples by ESI-MS (Figure S31, Supporting Information). Since our NCB constructs were much larger (45-nt long for the NC probe strand and 48-nt long for the activator strand) than the constructs used in previous studies involving ESI-MS analysis[7c,21] (10- to 26-nt-long), extensive cationic metal adduction during the ESI process prevented us from deciphering the exact silver stoichiometries in purified NCB samples. To circumvent this issue, an ion-pairing reagent, octylamine, was added to the ESI samples to suppress salt adduct formation.[22] Although the number of adducts was reduced, the addition of octylamine destabilized the duplex NCB structures. This generated highly polydisperse MS spectra that only provided us with rough estimates of silver stoichiometries in NCB duplexes (Figure S31, Supporting Information). Without knowing the exact silver stoichiometries and AgNC binding sites in a pair of POT, the proposed zipper-bag model is just one of the many possibilities behind POT formation (see Discussion section in Supporting Information). Our future work is to continue investigating binding footprints and silver stoichiometries in purified NCB samples.

3.2. In Silico Design of Bright NCBs Using Chip Screening Results and Machine-Learning Models

Since the results from our high-throughput screening (Table 1) could not be easily transformed into simple design rules, we took advantage of machine-learning algorithms to classify NCBs and uncover sequence features that give bright NCBs. Machine-learning approaches have previously helped identify sequence features in DNA hosts that preferentially stabilize bright AgNCs, establishing the first statistical model for rational design of AgNCs with desired colors.[8b,15a] However, such a model was built upon the emission properties of ≈2000 AgNCs sandwiched between two identical strands (8- to 16-mers).[15b] Our AgNCs were different, as each of them was stabilized within an 18-nt long activator and a 15-nt long C55. Although both robotic-well-plate studies[15b] (2000 short strands) and NGS screening (40 000 NCBs in this report) covered only a small fraction of the overall ligand composition spaces (10- and 18-mers, respectively), statistical models could be built based on these small fractions of data.

We extracted sequence features (which include motifs and motif locations) only from the bright activators in library_1. As the ranking of activators in the yellow–orange channel was quite different from that in the red channel (Figure S32A, Supporting Information), we performed separate trainings on yellow–orange and red NCBs. Following the approach proposed by Copp and Gwinn,[8b,15a,b] the top 30% NCBs (3600) were labeled as the "bright" class and the bottom 30% were labeled as the "dark" class. 339 and 567 features from the bright and dark classes in the yellow–orange channel (denoted as bright yellow–orange and dark yellow–orange features) and 402 and 1,164 features from the bright and dark classes in the red channel (denoted as bright red and dark red features) were separately identified by MERCI.[23] To decrease the chance of overfitting, we further narrowed down to a set of the most discriminative features with 61 bright yellow–orange, 121 dark yellow–orange, 103 bright red, and 112 dark red features using Weka[24] (Tables S14 and S15, Supporting Information, and Experimental Section). A feature vector was employed to describe the location of each activator in the high-dimensional space for classification model development (**Figure 4**A).

A number of models were established for classifying the chip screening results, based on algorithms such as logistic regression, linear discriminant analysis, decision tree, AdaBoost, and support vector machines (Table S13, Supporting Information). All models were built on "bright yellow–orange versus dark yellow–orange" or "bright red versus dark red" classification. To evaluate the model performance, we defined the accuracy of the model (Acc) as $(T_B + T_D)/(T_B + F_B + T_D + F_D)$, where T_B is the number of true predictions that the model makes for bright activators, T_D and F_D are the numbers of true and false dark predictions, and F_B is the number of false bright predictions. In other words, Acc represented the fraction of test sequences that the model correctly identifies as "bright" or "dark" activators. We found the model built on logistic regression has the best performance, achieving an average accuracy of 0.89 and 0.87 in the yellow–orange and red emission classification, respectively. In our model development process, the categorized dataset was divided into a training set (80% of the selected sequences) and
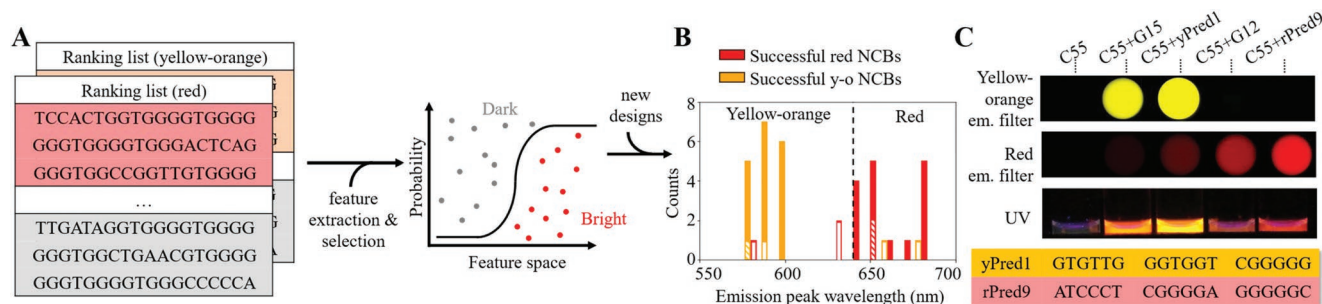
Figure 4. In silico design of bright yellow–orange and red NCBs based on machine learning results. A) From the chip selection results, we labeled the top 30% NCBs as 'bright' class and the bottom 30% as 'dark' class. The sequence features of these selected NCBs were then extracted by MERCI and selected by Weka. The resulting feature vectors thus defined the location of individual activators in the high-dimensional space. Several machine-learning models were tested for activator classification, among which the logistic regression had the best performance. B) 40 new activators were designed in silico and tested by fluorometry. Using 640 nm as the cutoff, the stacked histogram of NCB emission peaks showed two color bands. While 3 out of the 20 yellow–orange NCB candidates (y-o NCBs) showed low emission (enhancement ratio less than 66, Tables S11 and S12B, Supporting Information) or red emission (achieving 85% test-tube validation accuracy), 5 out of the 20 red NCB candidates showed either low emission (enhancement ratio less than 145, Tables S10 and S12A, Supporting Information) or yellow–orange emission peak. Hatched bars represent the failed designs with low emission. Empty bars represent the failed designs with wrong emission peaks. Dashed vertical line represents 640 nm. C) Plate-reader images acquired using yellow–orange (top) and red (bottom) excitation/emission filter sets, and the activator sequences of the two successfully predicted NCBs.

a test set (20% of the selected sequences). The selection process iterated five times while rotating the training set and the test set, resulting in a fivefold cross-validation that guarantees the model consistency (Figure S32,B,C Supporting Information). As expected, the propensity of an activator to be "bright" is not only determined by having "bright" motifs within the activator but also by positioning these motifs at proper locations.

Separately, based on the most discriminative features identified by Weka,[24] 1000 bright yellow–orange and 1000 bright red activator candidates were designed in silico (Figure S33, Supporting Information, and Experimental Section). In the high-dimensional space, we employed the minimal "edit distance"[15b,25] to identify the "closest" activator sequence in the library_1 dataset for each of the candidates. Consequently, when the closest library sequence was not among the top 200 bright activators screened, the candidate was discarded. Besides, when the candidate sequence had less than three or more than five single-base mutations, they were also discarded to restrict our search space. After going through these candidate refining steps, we were down to 100 bright yellow–orange and 54 bright red candidates. Among these candidates, the logistic regression model classified 85 and 41 of them as bright yellow–orange and red activators, respectively. From these most promising candidates, 20 were randomly selected, synthesized, hybridized with the C55 probes in test tubes, and measured by fluorometers.

Compared to the randomly generated activator sequences (Figure S34 and Table S9, Supporting Information), our design and classification pipeline produced new activators that were 8.5 times (85% vs 10%) and 1.9 times (75% vs 40%) more likely to be bright yellow–orange and red, respectively (Figures S35 and S36 and Tables S10 and S11, Supporting Information). Besides, the average enhancement ratio of in-silico-designed yellow–orange and red activators were 22 times and twice higher than that of random sequences, respectively (Table S9, Supporting Information). Moreover, while all random sequences gave more or less red emission, our pipeline successfully produced NCBs with yellow–orange emission (Figure 4B). In particular, among all bright candidates tested, we identified

a new yellow–orange activator (yPred1: GTGTTGGGTG-GTCGGGGG, with only 12 guanines) and a new red activator (rPred9: ATCCCTCGGGGAGGGGGC, with only 9 guanines) that were 2.13- and 1.30-fold brighter than the gold standards G15 and G12 in activating the C55 NC probe in test tubes, respectively (Figure 4C and Tables S10 and S11, Supporting Information).

4. Conclusion

We have performed high-throughput screening on more than 40 000 activators using repurposed NGS chips. Not only did we discover new NCBs (yAct1 and rAct1) that are two to three times brighter than the known best NCBs (G15 and G12, Figure 1), but we also identified a critical zone in the activator (positions 7–12) that stabilizes bright AgNC chromophores (Figure 2). In the search for the most extreme POT-NCBs, the chip platform helped identify a red pair (rPOT5-rPOT6) and a yellow–orange pair (yPOT5-yPOT6) with POT difference ratios as high as 9 and 31, respectively (Figure 3). By probing the NCBs at the near single-molecule level, we confirmed that the observed brightness difference at the ensemble level is attributed to the differences in the single-emitter brightness and the chromophore chemical yield (Figures S27 and S28, Supporting Information). Based on the findings of the critical zone (positions 7–12) and the POT hotspots (positions 2–4 for the red POTs and positions 4–6 for the yellow–orange POTs), we proposed a zipper-bag model that could explain how POT hotspots lead to the creation of distinct AgNC chromophores and alter the chromophore chemical yields (Figure 3). We emphasize that our zipper-bag model is only one of many possibilities. Further investigation on silver stoichiometries and AgNC footprints in purified NCBs using ESI-MS and a-EPD MS[19] is necessary to prove the zipper-bag model.

As the results from high-throughput screening could not be easily converted into simple rules for designing bright NCBs, we employed machine-learning algorithms to classify the

screening results and built a pipeline to design bright NCBs in silico. 40 new NCBs were generated by the pipeline, clearly showing two designated color bands (Figure 4). We also found that brighter NCBs could be achieved with fewer numbers of guanine bases in the activators. Although the overall sequence space investigated in this report (≈40 000 variants) represents a small fraction of the entire 18-mer space (4^{18} variants), our NGS platform has the scalability to broaden the search space by another one to three orders of magnitudes (by using a NextSeq or NovaSeq chip), thus leading to a more expansive machine-learning model in the future.

Our chip screening platform can facilitate the development of new chemical sensors based on DNA-templated AgNCs[26] or the study of other metal nanoclusters templated in DNA.[27] The chemical repertoire of natural nucleic acids can be expanded by connecting functional moieties to the alkyne-modified C5 site on dU,[28] thus allowing us to study the interactions between a wide variety of functional moieties and AgNCs on NGS chips. The discoveries of critical zones and interaction hotspots lead to the zipper-bag model, which provides us with a picture on how surrounding nucleobases can interact with the AgNCs encapsulated in NCBs and control their chemical yields and emission properties. Moreover, the knowledge of POTs can be directly applied to design new sensors for single-nucleotide polymorphism detection. To our knowledge, this article is the first report that shows NGS chips are repurposed for high-throughput screening of fluorescent nanomaterials. Our high-throughput screening and machine-learning-based design pipeline is not only accelerating the discovery of new NCBs for diverse applications, but also providing insights into the chemical yield and the emitter brightness controlled by the sequence features. We anticipate that new NCB-based sensors and new fluorescence barcodes will soon be developed based on the design strategy that we lay out in this report.

5. Experimental Section

Statistical Analysis: Fluorescence images collected for high-throughput screening were first aligned using the CHAMP program[14d] and alignment results were further analyzed using customized Python script. Fluorometry results were analyzed usin a customized Python script. POT results were expressed as mean ± standard deviation with three repeats. The statistical significance relating to NGS chip imaging results was performed by Mann–Whitney U-test. Differences were ranked significant when $*p < 0.05$, $**p < 0.01$, $***p < 0.001$.

Supporting Information

Supporting Information is available from the Wiley Online Library or from the author.

Acknowledgements

Conflict of Interest

The authors declare no conflict of interest.

Author Contributions

Y.-A.K., C.J., Y.-A.C., J.T.P., I.J.F., and H.-C.Y. discussed and defined the project. I.J.F. and H.-C.Y. supervised the research. Y.-A.K., C.J., Y.-A.C., O.S.Z., and T.N.D. prepared the NCBs and carried out the imaging experiments. Y.-A.K. and H.-C.K. prepared PCR samples for the *MiSeq* chip selection. Y.-A.K., O.S.Z., J.A.H., and J.R.R. wrote the image alignment and analysis software. Y.-A.K. and O.S.Z. wrote flat-field correction script. Y.-A.K., O.S.Z., D.C.W., and S.H. made a comparison on machine-learning algorithms and establish the in silico design workflow. Y.-A.K. and Y.-I.C. performed fluorometry data analysis. J.N.W., S.W.S., and J.S.B. conducted the mass spectrum experiments and analysis. Y.-A.K., I.J.F., and H.-C.Y. wrote the article with editorial assistance from all co-authors.

Data Availability Statement

The data that support the findings of this study are available from the corresponding author upon reasonable request.

Keywords

[1] a) H. Kobayashi, M. Ogawa, R. Alford, P. L. Choyke, Y. Urano, *Chem. Rev.* **2010**, *110*, 2620; b) A. B. Chinen, C. M. Guan, J. R. Ferrer, S. N. Barnaby, T. J. Merkel, C. A. Mirkin, *Chem. Rev.* **2015**, *115*, 10530.

[2] M. Rajendran, A. D. Ellington, *Nucleic Acids Res.* **2003**, *31*, 5700.

[3] H. C. Yeh, J. Sharma, J. J. Han, J. S. Martinez, J. H. Werner, *Nano Lett.* **2010**, *10*, 3106.

[4] J. M. Obliosca, M. C. Babin, C. Liu, Y. L. Liu, Y. A. Chen, R. A. Batson, M. Ganguly, J. T. Petty, H. C. Yeh, *ACS Nano* **2014**, *8*, 10150.

[5] H.-C. Yeh, J. Sharma, J. J. Han, J. S. Martinez, J. H. Werner, *IEEE Nanotechnol. Mag.* **2011**, *5*, 28.

[6] Y. S. Ang, W. W. E. Woon, L. Y. L. Yung, *Nucleic Acids Res.* **2018**, *46*, 6974.

[7] a) J. M. Obliosca, C. Liu, H. C. Yeh, *Nanoscale* **2013**, *5*, 8443; b) D. Schultz, K. Gardner, S. S. Oemrawsingh, N. Markesevic, K. Olsson, M. Debord, D. Bouwmeester, E. Gwinn, *Adv. Mater.* **2013**, *25*, 2797; c) S. M. Copp, D. Schultz, S. Swasey, J. Pavlovich, M. Debord, A. Chiu, K. Olsson, E. Gwinn, *J. Phys. Chem. Lett.* **2014**, *5*, 959; d) J. T. Petty, O. O. Sergev, M. Ganguly, I. J. Rankine, D. M. Chevrier, P. Zhang, *J. Am. Chem. Soc.* **2016**, *138*, 3469; e) D. J. E. Huard, A. Demissie, D. Kim, D. Lewis, R. M. Dickson, J. T. Petty, R. L. Lieberman, *J. Am. Chem. Soc.* **2019**, *141*, 11465; f) C. Cerretani, H. Kanazawa, T. Vosch, J. Kondo, *Angew. Chem., Int. Ed.* **2019**, *58*, 17153.

[8] a) H. C. Yeh, J. Sharma, M. S. Ie, D. M. Vu, J. S. Martinez, J. H. Werner, *J. Am. Chem. Soc.* **2012**, *134*, 11550; b) S. M. Copp, P. Bogdanov, M. Debord, A. Singh, E. Gwinn, *Adv. Mater.* **2014**, *26*, 5839; c) S. Juul, J. M. Obliosca, C. Liu, Y. L. Liu, Y. A. Chen, D. M. Imphean, B. R. Knudsen, Y. P. Ho, K. W. Leong, H. C. Yeh,

Nanoscale **2015**, *7*, 8332; d) Y. A. Chen, J. M. Obliosca, Y. L. Liu, C. Liu, M. L. Gwozdz, H. C. Yeh, *J. Am. Chem. Soc.* **2015**, *137*, 10476; e) J. T. Petty, M. Ganguly, A. I. Yunus, C. He, P. M. Goodwin, Y.-H. Lu, R. M. Dickson, *J. Phys. Chem. C* **2018**, *122*, 28382; f) Y. A. Chen, H. T. Vu, Y. L. Liu, Y. I. Chen, T. D. Nguyen, Y. A. Kuo, S. Hong, Y. A. Chen, S. Carnahan, J. T. Petty, H. C. Yeh, *Chem. Commun.* **2019**, *55*, 462.

[9] J. Zhang, C. Li, X. Zhi, G. A. Ramón, Y. Liu, C. Zhang, F. Pan, D. Cui, *Anal. Chem.* **2015**, *88*, 1294.

[10] J. J. Li, X. Q. Zhong, H. Q. Zhang, X. C. Le, J. J. Zhu, *Anal. Chem.* **2012**, *84*, 5170.

[11] M. Zhang, S. M. Guo, Y. R. Li, P. Zuo, B. C. Ye, *Chem. Commun.* **2012**, *48*, 5488.

[12] J. Yin, X. He, K. Wang, F. Xu, J. Shangguan, D. He, H. Shi, *Anal. Chem.* **2013**, *85*, 12011.

[13] C. I. Richards, S. Choi, J.-C. Hsiang, Y. Antoku, T. Vosch, A. Bongiorno, Y.-L. Tzeng, R. M. Dickson, *J. Am. Chem. Soc.* **2008**, *130*, 5038.

[14] a) R. Nutiu, R. C. Friedman, S. Luo, I. Khrebtukova, D. Silva, R. Li, L. Zhang, G. P. Schroth, C. B. Burge, *Nat. Biotechnol.* **2011**, *29*, 659; b) J. M. Tome, A. Ozer, J. M. Pagano, D. Gheba, G. P. Schroth, J. T. Lis, *Nat. Methods* **2014**, *11*, 683; c) J. D. Buenrostro, C. L. Araya, L. M. Chircus, C. J. Layton, H. Y. Chang, M. P. Snyder, W. J. Greenleaf, *Nat. Biotechnol.* **2014**, *32*, 562; d) C. Jung, J. A. Hawkins, S. K. Jones, Jr., Y. Xiao, J. R. Rybarski, K. E. Dillard, J. Hussmann, F. A. Saifuddin, C. A. Savran, A. D. Ellington, A. Ke, W. H. Press, I. J. Finkelstein, *Cell* **2017**, *170*, 35; e) C. J. Layton, P. L. McMahon, W. J. Greenleaf, *Mol. Cell* **2019**, *73*, 1075.

[15] a) S. M. Copp, A. Gorovits, S. M. Swasey, S. Gudibandi, P. Bogdanov, E. G. Gwinn, *ACS Nano* **2018**, *12*, 8240; b) S. M. Copp, S. M. Swasey, A. Gorovits, P. Bogdanov, E. G. Gwinn, *Chem. Mater.* **2019**, *32*, 430; c) A. Gonzàlez-Rosell, C. Cerretani, P. Mastracco, T. Vosch, S. M. Copp, *Nanoscale Adv.* **2021**, *3*, 1230.

[16] S. L. Hayward, P. E. Lund, Q. Kang, A. Johnson-Buck, M. Tewari, N. G. Walter, *J. Am. Chem. Soc.* **2018**, *140*, 11755.

[17] a) S. M. Swasey, L. E. Leal, O. Lopez-Acevedo, J. Pavlovich, E. G. Gwinn, *Sci. Rep.* **2015**, *5*, 10163; b) J. Kondo, Y. Tada, T. Dairaku, Y. Hattori, H. Saneyoshi, A. Ono, Y. Tanaka, *Nat. Chem.* **2017**, *9*, 956.

[18] a) J. Sharma, H. C. Yeh, H. Yoo, J. H. Werner, J. S. Martinez, *Chem. Commun.* **2010**, *46*, 3280; b) H.-C. Yehih, J. Sharma, H. Yoo, J. S. Martinez, J. H. Werner, *Proc. SPIE* **2010**, *7576*, 75760N.

[19] M. S. Blevins, D. Kim, C. M. Crittenden, S. Hong, H. C. Yeh, J. T. Petty, J. S. Brodbelt, *ACS Nano* **2019**, *13*, 14070.

[20] J. T. Petty, M. Ganguly, I. J. Rankine, D. M. Chevrier, P. Zhang, *J. Phys. Chem. C* **2017**, *121*, 14936.

[21] a) P. R. O'Neill, L. R. Velazquez, D. G. Dunn, E. G. Gwinn, D. K. Fygenson, *J. Phys. Chem. C* **2009**, *113*, 4229; b) D. Schultz, E. G. Gwinn, *Chem. Commun.* **2012**, *48*, 5748.

[22] a) A. C. McGinnis, E. C. Grubb, M. G. Bartlett, *Rapid Commun. Mass Spectrom.* **2013**, *27*, 2655; b) M. Scalabrin, M. Palumbo, S. N. Richter, *Anal. Chem.* **2017**, *89*, 8632; c) J. M. Sutton, M. G. Bartlett, *Rapid Commun. Mass Spectrom.* **2020**, *34*, e8696; d) J. M. Sutton, N. M. El Zahar, M. G. Bartlett, *J. Am. Soc. Mass Spectrom.* **2021**, *32*, 497.

[23] C. Vens, M. N. Rosso, E. G. Danchin, *Bioinformatics* **2011**, *27*, 1231.

[24] M. Hall, E. Frank, G. Holmes, B. Pfahringer, P. Reutemann, I. H. Witten, *ACM SIGKDD Explor. Newsl.* **2009**, *11*, 10.

[25] E. S. Ristad, P. N. Yianilos, *IEEE Trans. Pattern Anal. Mach. Intell.* **1998**, *20*, 522.

[26] J. T. D. Bonis-O'Donnell, A. Thakrar, J. W. Hirschberg, D. Vong, B. N. Queenan, D. K. Fygenson, S. Pennathur, *ACS Chem. Neurosci.* **2018**, *9*, 849.

[27] a) W. Y. Chen, G. Y. Lan, H. T. Chang, *Anal. Chem.* **2011**, *83*, 9450; b) X. Jia, J. Li, L. Han, J. Ren, X. Yang, E. Wang, *ACS Nano* **2012**, *6*, 3311; c) J. Chen, X. Ji, P. Tinnefeld, Z. He, *ACS Appl. Mater. Interfaces* **2016**, *8*, 1786.

[28] a) A. Drees, M. Fischer, *Int. J. Mol. Sci.* **2021**, *22*, 9202; b) D. Wu, T. Feagin, P. Mage, A. Rangel, L. Wan, A. Li, J. Coller, M. Eisenstein, S. Pitteri, H. T. Soh, *bioRxiv* **2020**, https://doi.org/10.1101/2020.04.25.060004.